

Detection of Non-metallic Inclusions in Steel Continuous Casting Billets

YING REN, YUFENG WANG, SHUSEN LI, LIFENG ZHANG, XIANGJUN ZUO, SIMON N. LEKAKH, and KENT PEASLEE

This work applied automated particle analysis to study non-metallic inclusions in steel. Compared with traditional methods, the approach has the advantage of capturing the morphology, measuring the size, recording the original positions, and identifying the composition of inclusions on a selected area in a short time. The morphology and composition of typical inclusions were analyzed using partial acid extraction and discussed through thermodynamic calculation. Steel samples were collected from the entire cross section of billets cast during times of steady state and ladle change. The spatial distribution of inclusions agreed well with the measurement of the total oxygen. The spatial distribution of inclusions was plotted to represent the entrapment positions of inclusions on the casting strand and their concentration on the cross section of the billet. Also, regarding the different size and type of inclusions, the spatial distribution of classified inclusions was explored such as the distribution of sulfide, oxide, and high sodium and potassium content inclusions. The sufficient information could be used to identify the source of inclusions and guide the steel refining process.

DOI: 10.1007/s11663-014-0042-y

© The Minerals, Metals & Materials Society and ASM International 2014

I. INTRODUCTION

CHARACTERIZING non-metallic inclusions is one of the most important aspects to assuring clean steel. Inclusions remaining in the final product can damage steel properties and degrade its quality.^[1,2] To produce high-performance steel, non-metallic inclusions must be controlled. Generally, non-metallic inclusions can be classified as either indigenous or exogenous. Indigenous inclusions are a result of alloying elements within the steel reacting with dissolved gas (generally oxygen) to form solid inclusions in the cast steel. The inclusion could be formed during deoxidation, reoxidation, or solidification from reduced gas species solubility in the solid state. Exogenous inclusions come from sources outside the liquid steel, such as slag entrainment or refractory damage. The evaluation of non-metallic inclusions in steel is of great interest to metallurgists and materials scientists and includes exploring the total

amount, morphology, size distribution, and spatial distribution of inclusions; and identifying their chemical composition. The research group of the current author has extensively investigated the different aspects of inclusions, including the experimental investigation, industrial trials, modeling, and literature review.^[1,3-12]

Zhang and Thomas^[1] reviewed more than twenty methods of evaluating impurities and inclusions in steel. Among these methods, a metallographic microscope^[13] is widely applied to explore the two-dimensional morphology and size of inclusions in steel. However, it cannot identify the chemical composition of inclusions. Scanning electron microscopy^[14] permits exploration of morphology of inclusions in the microscale. Further, by coupling with energy-dispersive spectroscopy, scanning electron microscopy permits identification of the elemental composition of inclusions and their relative proportions. Counting a large number of inclusions with this method, however, is too time-intensive to be practical. Acid extraction method can obtain the stereoscopic morphology of inclusions, but destroy sulfide inclusions.^[15-18] For the extraction using bromine-methanol, iron bromide dissolves readily and in the electrolytic approach, in general, a chelant must be added to dissolved the iron, which helps to reveal the three-dimensional morphology and keep original composition of the inclusions.^[19] Ultrasonic inspection^[20,21] and X-ray detection^[22] are more efficient than these methods, and can be employed for online analysis; however, the morphology and composition data are difficult to obtain. Other indirect methods, like total oxygen (T.O.) measurement^[23,24] or continuous excitation of spark spectrum, have the limitations to determine both the distribution and the composition of inclusions.^[25,26]

YING REN, Ph.D. Student, and LIFENG ZHANG, Professor, are Beijing Key Laboratory of Green Recycling and Extraction of Metals (GREM) and School of Metallurgical and Ecological Engineering, University of Science and Technology Beijing, No. 30, Xueyuan Road, Haidian District, Beijing 100083, P.R. China. Contact e-mail: zhanglifeng@ustb.edu.cn YUFENG WANG, Engineer, is with the R&D Group, SSAB, Muscatine, IA. SHUSEN LI, Assistant General Manager, Qian'an Steelmaking Co. Ltd., Shougang Group, Qian'an 064404, Hebei, P.R. China. XIANGJUN ZUO, Engineer, is with the Continuous Casting Department, CISDI Engineering Co. Ltd., Chongqing, P.R. China. SIMON N. LEKAKH, Research Professor, and KENT PEASLEE, Professor, are with the Department of Materials Science & Engineering, Missouri University of Science and Technology (Missouri S&T), Rolla, MO.

Manuscript submitted June 28, 2011.

Table I. Chemical Composition of the Steel (Percentage)

C	Si	Mn	S	Ti	Mg	Al	Ca
0.20	0.23	0.48	0.006	0.002	0.0006	0.011	0.0002

In the present study typical inclusions after different time acid extractions in steel continuous casting billets were observed, which was in accordance with thermodynamic calculation. Moreover, the size distribution, spatial distribution, and composition of non-metallic inclusions in steel continuous casting billets were investigated using automatic particle analyzer—ASPEX. This method permits quick determination of the morphology, size distribution, spatial distribution, and composition of all inclusions in a selected area. The inclusions results were compared with measured total oxygen analyzed by a Leco oxygen analyzer.

II. METHODOLOGY

A. Experimental Procedures

Billet samples were obtained from an industrial plant casting aluminum-killed medium carbon steel in a four strand, $150 \times 150 \text{ mm}^2$ billet caster. The composition of the steel produced is given in Table I. The tundish was lined with refractory material high in magnesium oxide with vertical straight nozzles submerged 100 mm below the meniscus of the mold. The casting speed was 1.5 to 2.0 m/min resulting in a standard casting time of about 45 minutes per heat with 2 to 3 minutes required to change a ladle. A casting sequence typically pours 4 to 6 heats with 60 ton per heat, depending on the lifetime of the submerged entry nozzle and the casting schedule.

Billets samples were collected at both steady state and unsteady state. One sample was taken from the second strand of the billet caster after 3 heats of pouring at a casting speed of 1.5 to 1.7 m/min to represent the steady-state (S1) operation. Another sample was obtained during ladle change to reflect the unsteady state of the casting process (S2). These samples were cut into sections, as shown in Figure 1. A billet section 5 mm in thickness was used for oxygen analysis to map the three-dimensional distribution of oxide inclusions over the billet cross section.

For the oxygen samples, a 5-mm-thick billet slice was sawed into 45 rectangle samples with the dimension of $30 \times 15 \times 5 \text{ mm}^3$, as shown in Figure 2(a). Each sample was machined into three cylindrical samples, with a diameter of 5 mm for the oxygen analyzer. For the metallographic sample, a 20 mm billet slice was divided into 49 samples, each measuring 20 mm by 20 mm, as illustrated in Figure 2(b).

B. Analysis Methods

The analysis of oxygen was performed using a Leco Oxygen Analyzer in which the sample was melted inside a graphite crucible and the product gas quantified by a detector and converted to the total oxygen content. The

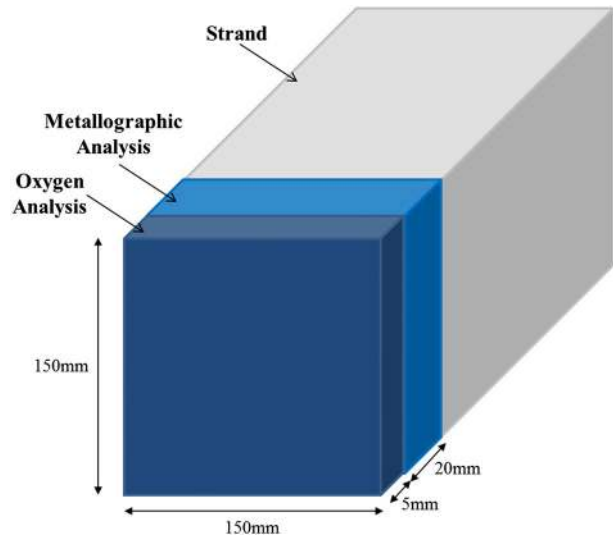


Fig. 1—Sampling from a steel billet.

observation of inclusions was performed using an automated SEM-EDS—ASPEX 1020 system.^[27] The automated particle analysis is a frame-based analysis. First, a selected area was divided into several small fields under the microscope. A focused electron beam was positioned on one field, and the microscope did a fast search of the field with large search steps. The intensity of the back-scatter electrons was then recorded and transferred to a computer. Once a particle was found based on thresholding of the intensity of the back-scatter electrons, the step size was reduced to measure more precisely the dimensions of the particle. The center of the particle was identified using a bisected chord method, and the rotating chord algorithm was employed to measure the particle. Finally, the beam was again positioned in the center of the particle to acquire the characteristic X-ray. After combination of these steps in one field, the beam moved to other fields and repeated the analysis.^[28,29]

In the present study, using ASPEX 1020 system, the size distribution, composition, and rough morphology are automatically obtained. Although the images of inclusions obtained using ASPEX are not high in resolution, the ASPEX has the advantage of fast scanning and automatic feature analysis resulting in a large number of particles in a sample being analyzed in several hours. A sample measuring $20 \times 20 \text{ mm}^2$ was selected for analysis on each metallographic specimen and the electron beam scanned the random area on the $20 \times 20 \text{ mm}^2$ sample until a 9.8 mm^2 scanned area was analyzed. The minimum particle size was set at $0.6 \mu\text{m}$, which means that the ASPEX 1020 was sensitive to only inclusions larger than $0.6 \mu\text{m}$. The types of inclusions were categorized according to the weight percentage of

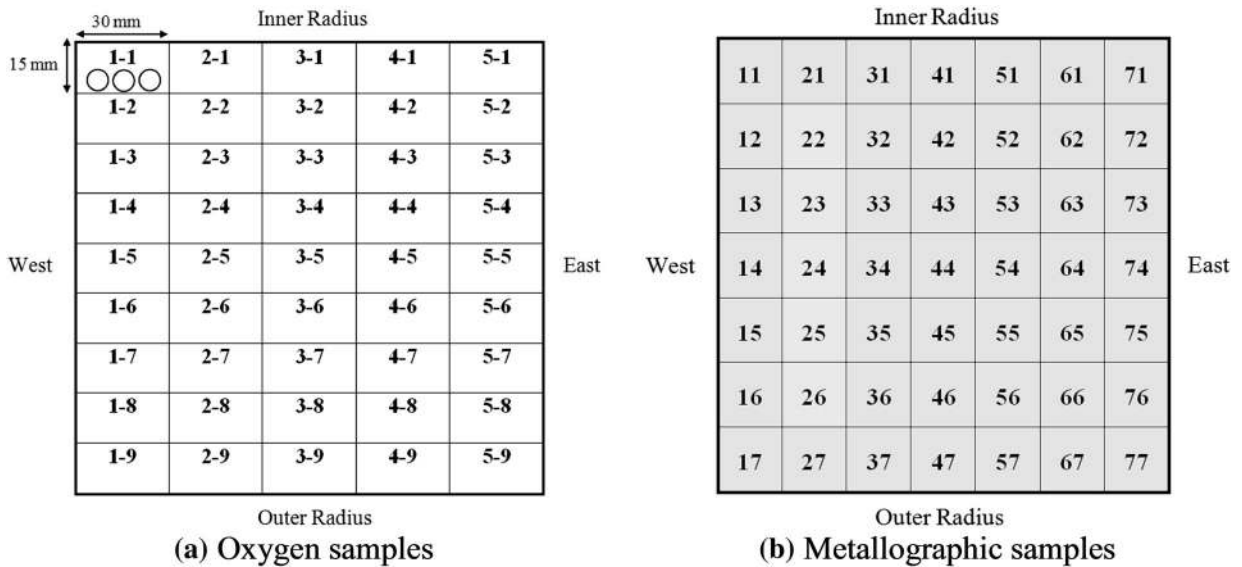


Fig. 2—Sample preparation.

Table II. Inclusions Classification Rules (Weight Percentage)

FeO stain/spots/pollution	Fe \geq 30 and O \geq 2.5
Microdefects	Fe \geq 97 and O $<$ 2.5
MnS	Mn $>$ 30 and S $>$ 20
CaS	Ca $>$ 30 and S $>$ 20
Ca-Mn-S	Ca $>$ 10, Mn $>$ 10, and S $>$ 20
Other sulfides	S $>$ 20
Al ₂ O ₃	Al $>$ 20, Mn $<$ 20, Ca $<$ 10, Si $<$ 20, S $<$ 20, and Mg $<$ 5
MgO	Mg $>$ 5, Al $<$ 10, Mn $<$ 20, Ca $<$ 10, Si $<$ 20, and S $<$ 20
Al-Mg-O	Mg $>$ 5, Al $>$ 10, Mn $<$ 20, Ca $<$ 10, Si $<$ 20, and S $<$ 20
CaO	Ca $>$ 20, S $<$ 20, Al $<$ 10, Si $<$ 20, Mn $<$ 20, and Mg $<$ 5
Ca-Al-O	Ca $>$ 10, Al $>$ 10, Si $<$ 20, Mn $<$ 20, Mg $<$ 5, and S $<$ 20
Ca-Mg-Al-O	Ca $>$ 10, Mg $>$ 5, Al $>$ 10, S $<$ 20, Si $<$ 20, and Mn $<$ 20
SiO ₂	Si $>$ 20, Mn $<$ 20, Al $<$ 10, Ca $<$ 20, and S $<$ 20
MnO	Mn $>$ 20, Al $<$ 20, S $<$ 20, and Si $<$ 20
Mn-Si-O	Mn $>$ 20, Si $>$ 10, Al $<$ 10, and S $<$ 20
Mn-Al-O	Mn $>$ 20, Al $>$ 10, S $<$ 20, and Si $<$ 20
ZrO ₂	Zr $>$ 10, Al $<$ 10, Ca $<$ 20, Si $<$ 20, S $<$ 20, and Mn $<$ 20
TiO ₂	Ti $>$ 20, Al $<$ 10, Ca $<$ 20, Si $<$ 20, Mn $<$ 20, and S $<$ 20
Na ₂ O + K ₂ O	Na + K $>$ 3

elements detected in them. The rule file is shown in Table II. In order to observe the three-dimensional morphologies of inclusions, typical morphologies of inclusions were revealed using partial acid extraction. A 36 pct HCl solution was used as the solvent. Morphologies and compositions of inclusions on a steel sample ($32 \times 25 \times 15 \text{ mm}^3$) at different extraction times were compared.

III. MORPHOLOGY AND COMPOSITION OF INCLUSIONS

Figure 3 shows the typical morphology and composition of inclusions in the billet sample, which clearly

indicates the morphology of inclusions by ASPEX (Figure 3). The typical inclusions in the steel billets are alumina-based clusters, alumina magnesia ($\text{Al}_2\text{O}_3\text{-MgO}$) spinel single or cluster inclusions, silicon oxide (SiO_2) bearing spherical inclusions, separate sulfide-based inclusions, and irregularly shaped slag inclusions containing calcium oxide (CaO), potassium oxide (K_2O), and sodium oxide (Na_2O). Alumina (Al_2O_3) inclusions mainly stem from deoxidation by aluminum or reoxidation of the residual aluminum in the steel. Inclusions high in magnesium oxide are a result of the reaction between molten steel and magnesium refractory, especially the tundish lining refractory. Inclusions with sodium (Na) and potassium (K) are from the entrainment of the mold slag. Sulfide inclusions mainly

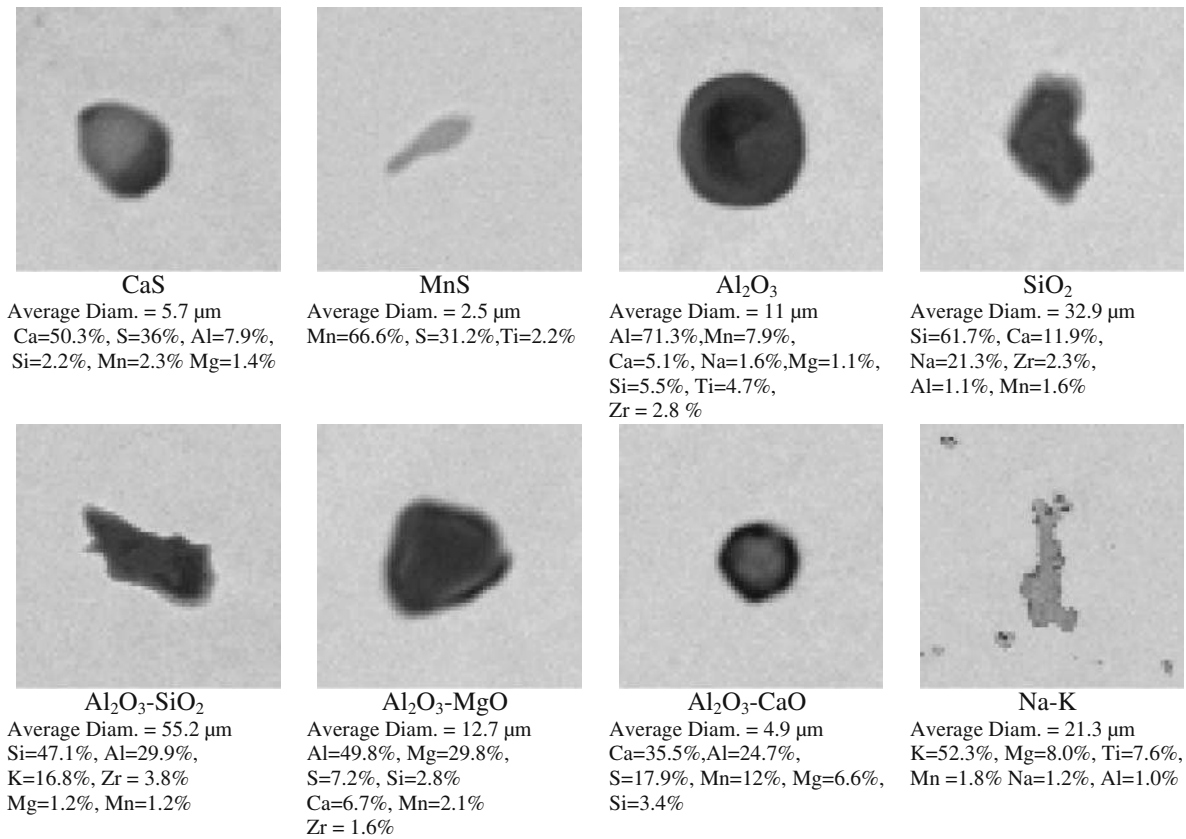


Fig. 3—Inclusion morphology and composition (in mass pct) observed by SEM (polished sample).

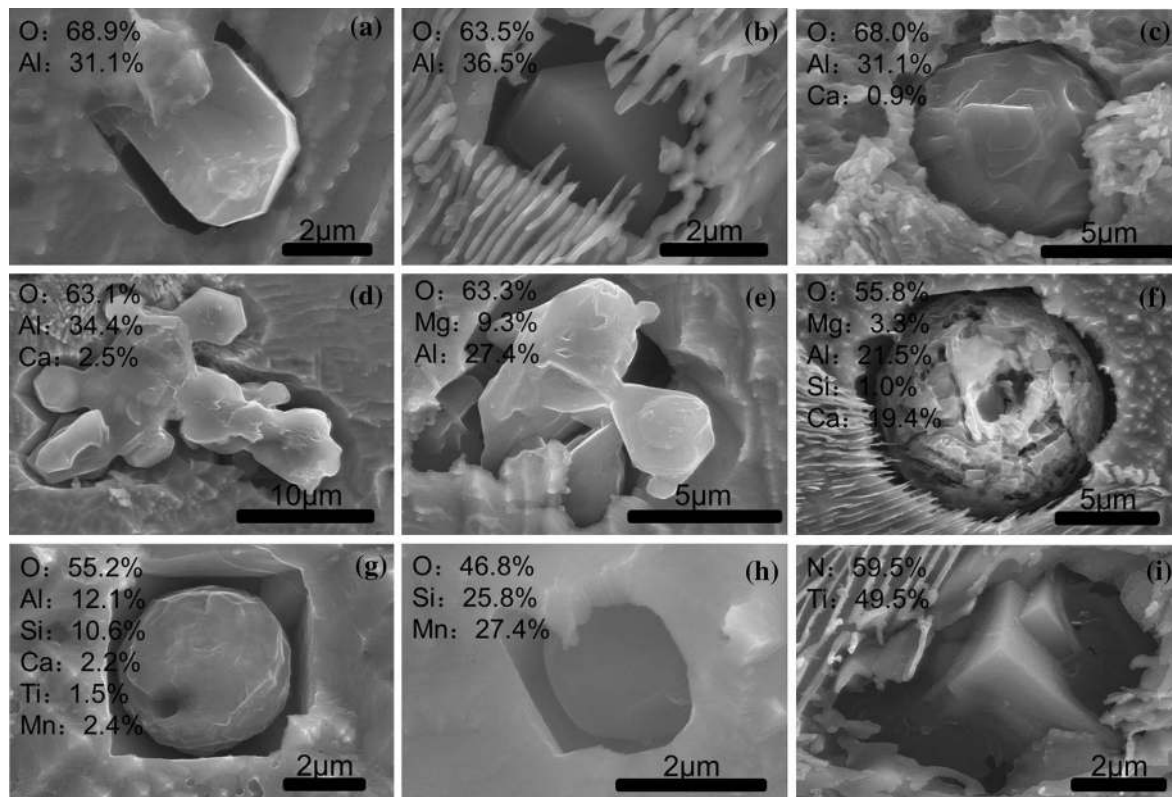


Fig. 4—Inclusion morphology and composition (atomic pct) observed by SEM (etched by acid).

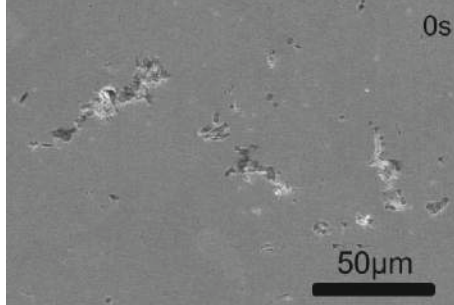
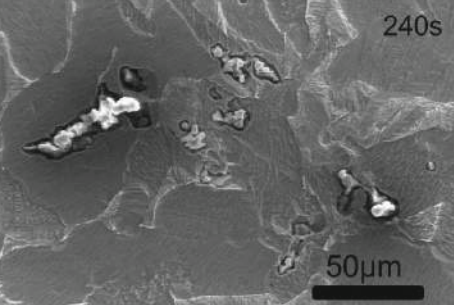
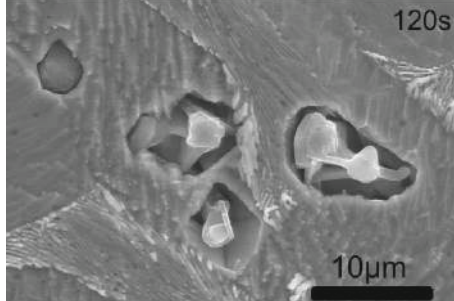
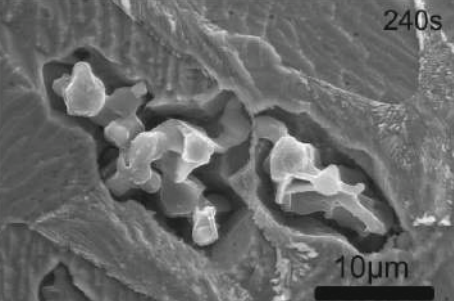
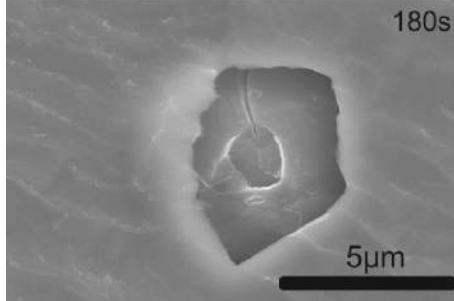
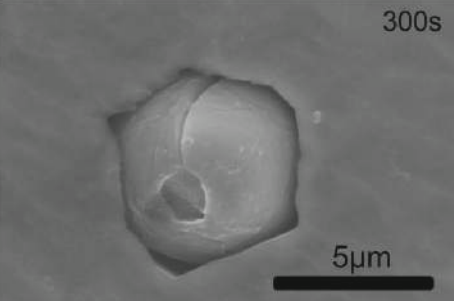
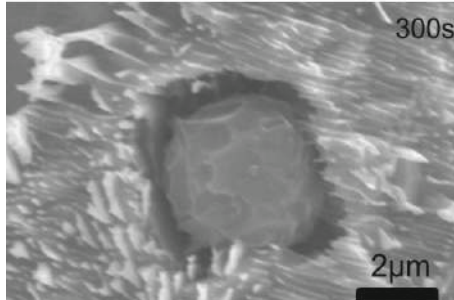
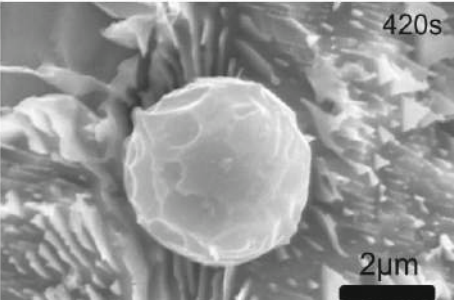
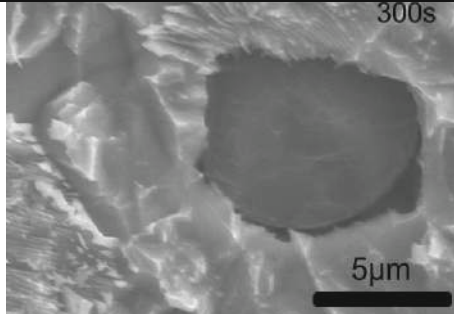
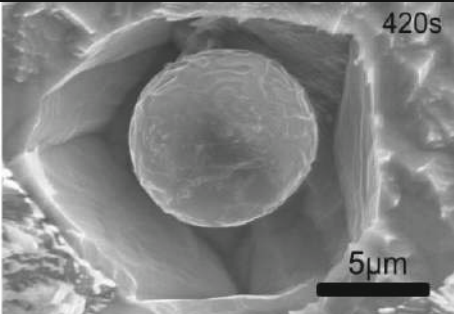
No.	Compositions (atom %)	Inclusions after different time acid extraction	
(a)	O : 69.1% Al : 28.0% Ca : 2.9%	 0s 50µm	 240s 50µm
(b)	O : 67.2% Mg : 6.0 Al : 25.9% Ca : 0.9%	 120s 10µm	 240s 10µm
(c)	O : 60.0% Al : 39.1% Ca : 0.9%	 180s 5µm	 300s 5µm
(d)	O : 58.5% Al : 26.2% Ca : 15.3%	 300s 2µm	 420s 2µm
(e)	O : 68.8% Al : 8.7% Si : 15.0% Mn : 7.4%	 300s 5µm	 420s 5µm

Fig. 5—Typical inclusions after different time acid extractions (the numerical value in the top right corner is the acid extraction acid time).

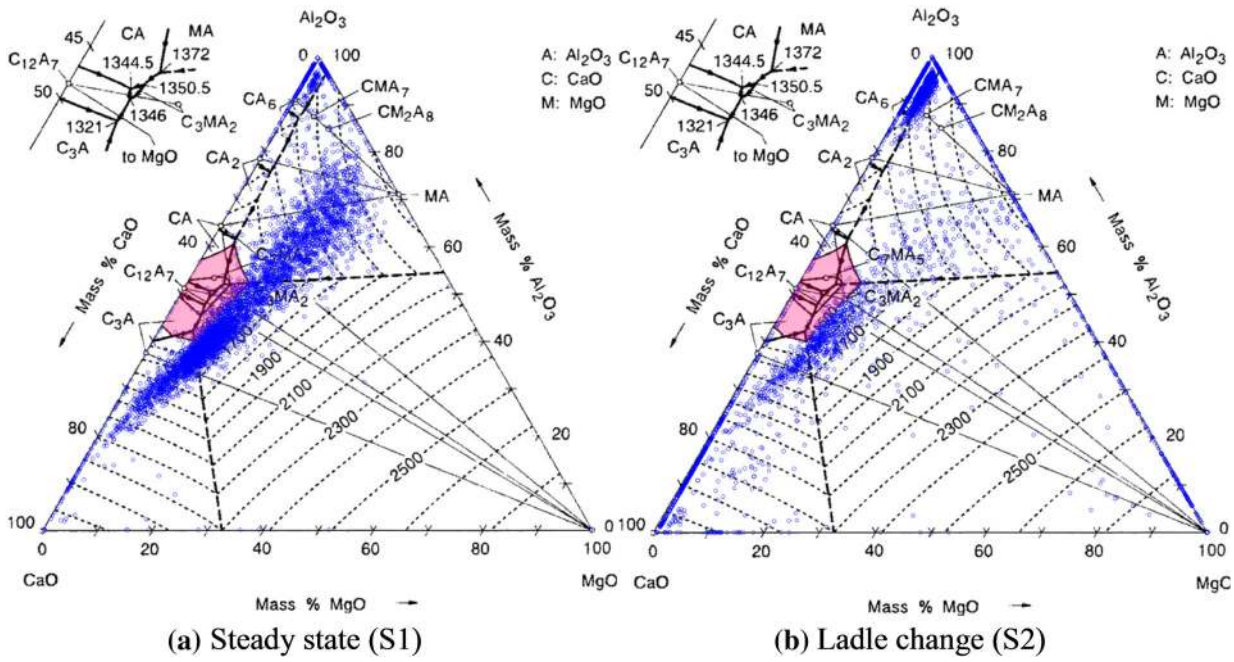


Fig. 6—Al₂O₃-CaO-MgO inclusions in steel.



Fig. 7—Clogging materials (mainly Al₂O₃-CaO-MgO inclusions) at the submerged entry nozzle.

precipitate during cooling and solidification of the steel. The optical resolution from ASPEX was set for providing sufficient information to determine the diameter, area, and perimeter of inclusions with reasonable

analytical time and storage space for thousands of counted inclusions.

The morphology and composition of typical inclusions etched by acid were detected using SEM-EDS

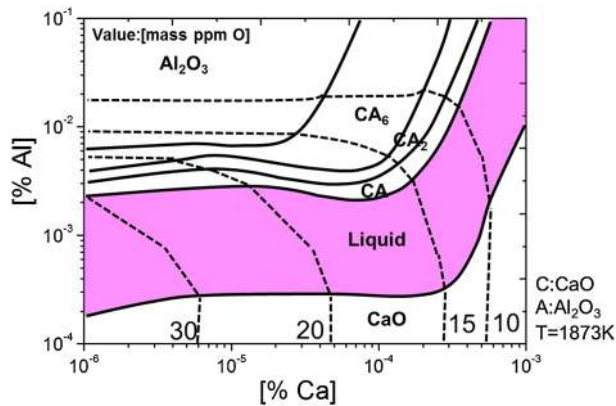


Fig. 8—Calculated stability diagram of Al-Ca-O system in the molten steel at 2146 K (1873 °C).

(Figure 4). Figures 4(a) through (d) are plate-like, angular, spherical, and irregular Al_2O_3 -based inclusions. Precipitation of different shape individual alumina particles along with the decrease of supersaturation degree of deoxidizing elements in the initial stage of holding time after deoxidation occurred.^[18] Meanwhile, plenty of Al_2O_3 -MgO spinel inclusions were generated, as shown in Figure 4(e). There were spherical calcium aluminate and silicon aluminate inclusions (Figures 4(f) and (g)). Spherical Si-Mn-O inclusions and hexahedral-like TiN inclusions were also found, as shown in Figures 4(h) and (i). After the acid extraction, CaS and MnS disappeared since sulfide reacted with the acid.^[15,17]

The three-dimensional morphologies of inclusions were revealed using partial acid extraction (Figure 5). After acid extraction, separate Al_2O_3 and Al_2O_3 -MgO single particles were revealed to big clustered inclusions (Figures 5(a) and (b)). In Figure 5(c), the diameter of spherical Al_2O_3 -based inclusions after 300s acid extraction was larger than that under 180s acid extraction condition. Inclusions of Al_2O_3 -CaO and Al-Si-Mn-O shown in Figures 5(d) and (e) were nearly spherical due to the fact that their melting temperature was lower than the temperature of the molten steel.

Figure 6 shows the ternary diagram of oxides based on the chemical composition of Al_2O_3 , CaO, and MgO. Each individual spot in this ternary diagram represents the composition of an inclusion. In continuous casting, solid particles can attach to the nozzle and may block the path of the molten steel. To prevent nozzle clogging, inclusions should be in the liquid state. However, the composition distribution indicates that most inclusions were solid under casting temperature. Only a few were in the liquid state, as illustrated by the shaded region [temperature <1773 K (1500 °C)] in the ternary diagram. The samples from both steady state (S1) and ladle change (S2) show that many particles were close to the Al_2O_3 region. Excess MgO would raise the melting point of inclusions. Several inclusions on the ternary diagram had magnesium oxide contents greater than 30 pct, indicating that the melting temperature of these particles was over 2573 K (2300 °C), and thus these inclusions were solid throughout the casting process. Since many

of the inclusions were compositions with high melting points, the submerged entry nozzle was seriously clogged in the industrial trial, as shown in Figure 7, resulting in early termination of casting.

Figure 8 shows the calculated stability diagram of Al-Ca-O system in the molten steel at 2146 K (1873 °C), which gives the stability regions for various inclusions at equilibrium as a function of [Al], [Ca], and [O] on the molten steel. The equilibrium constant $\log K$ of the reactions and the interaction activity coefficient were different from each other in the literatures,^[30–34] assuming unity activity of the oxide products. The values near the dotted circles show the oxygen content [mass ppm O]. To avoid nozzle clogging, the [Ca] and [Al] content of steel should be controlled within the shade liquid region in Figure 8. Among the various Al-Ca-O inclusions, only Al_2O_3 -3CaO and $7\text{Al}_2\text{O}_3$ -12CaO inclusions are liquid at 2146 K (1873 °C). The [Ca] and [Al] contents of the steel shown in Table I were located in the Al_2O_3 -rich region, indicating that the calcium treatment during the ladle refining in the current industrial trial was insufficient and more Ca-Si wire was needed.

The Equilibrium precipitation of inclusions during solidification of steel with a composition of Fe-0.2C-0.23Si-0.48Mn-0.006S-0.002Ti-0.0006Mg-0.0018O-0.007N-0.011Al-Ca (in mass pct) was calculated using the thermodynamic software, FACTSAGE (version 6.4) using “FACT53”, “Ftoxid,” and “FSstel” databases^[35] and is shown in Figure 9. When [Ca] in the steel was 2 ppm (Figure 9(a)), inclusions were mainly spinel and hardly liquid in the molten steel and they caused clogging of the submerged entry nozzle during continuous casting. During solidification of the steel, liquid inclusions were converted to $\text{CaMg}_2\text{Al}_6\text{O}_{27}$ and CaS. After the temperature reached approximately 1573 K (1300 °C), plenty of MnS and small amounts of TiN inclusions would be precipitated. With [Ca] content reaching 5 ppm first and then to 10 ppm (Figures 9(b) and (c)), the amount of spinel inclusions decreased and then disappeared, and there were only liquid inclusions in the molten steel. The inclusions of MnS were modified to CaS by the calcium treatment. If more calcium was added (Figures 9(d) and (e)), both CaS and liquid inclusions were generated in molten steel, and CaS would possibly clog the submerged entry nozzle at this condition. Therefore, the lack of control of the composition of inclusions during steel-making and refining has a catastrophic consequence on the casting process.

IV. SIZE AND SPATIAL DISTRIBUTION OF INCLUSIONS IN BILLETS

A. Size Distribution of Inclusions

Figure 10 shows the two-dimensional size distribution of the oxide inclusions directly obtained from the inclusion size measurement by ASPEX. Most of the inclusions in the billets were 0.6 to 5.0 μm . Inclusions larger than 20 μm were typically complex and stemmed from the refractory lining, entrained slag, or a combination of deoxidation and reoxidation products.^[7] These

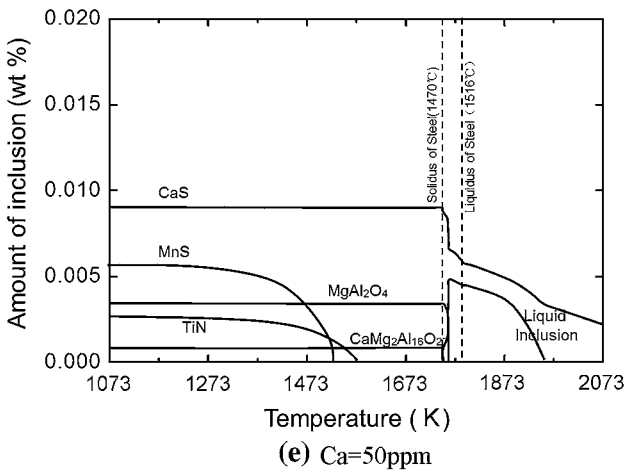
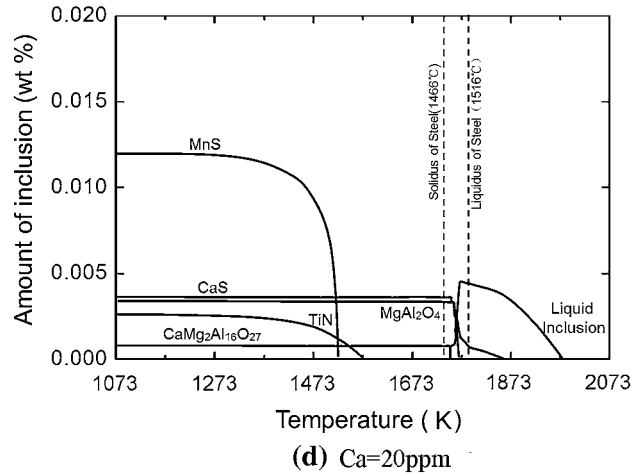
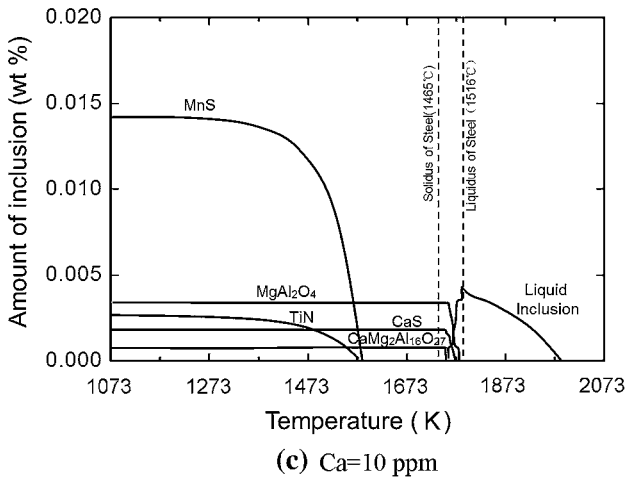
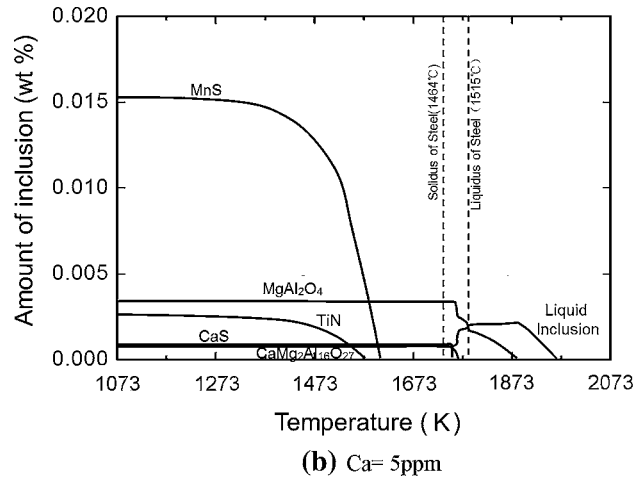
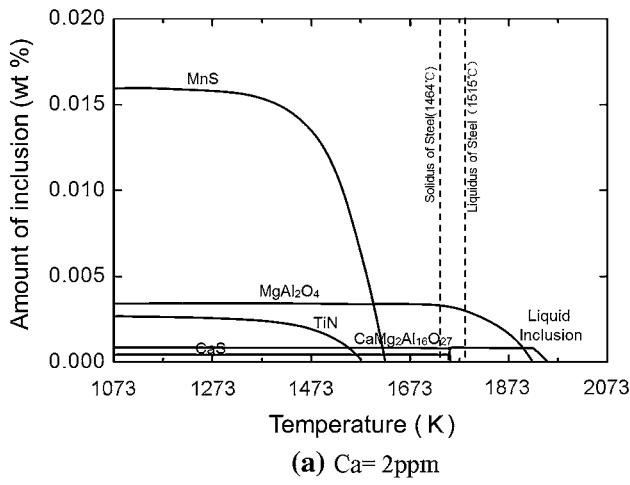


Fig. 9—Equilibrium precipitation of inclusions during solidification for steel of composition: Fe-0.2C-0.23Si-0.48Mn-0.006S-0.002Ti-0.0006Mg-0.0018O-0.007N-0.011Al-Ca in mass pct.

large inclusions are particularly harmful to the mechanical properties, acting as stress concentrators or causing surface cracking. Figure 10 indicates that there were more $>20 \mu\text{m}$ inclusions measured on the cross section of the billet during ladle change (S2) than that at the steady state (S1) due to the fact that more slag was entrained and more air was absorbed at the unsteady state than steady state.

B. Spatial Distribution of Inclusions

The distribution of inclusions with various compositions in the billet had special significance and it provided information about the distribution of alumina-based inclusions stemming from deoxidation,^[18,36] reoxidation,^[37] entraining refining slag,^[38] or refractory materials.^[39,40]

The inclusions of Na/K-bearing were from mold slag entrainment^[1]; most of sulfide precipitated during the cooling and solidification of the steel.^[41] The distribution of sulfide inclusions and oxide inclusions on the billet cross section as measured with the ASPEX inclusion analyzer is shown in Figures 11 and 12, respectively, which are based on the number fraction. On the billet cross section under steady casting state

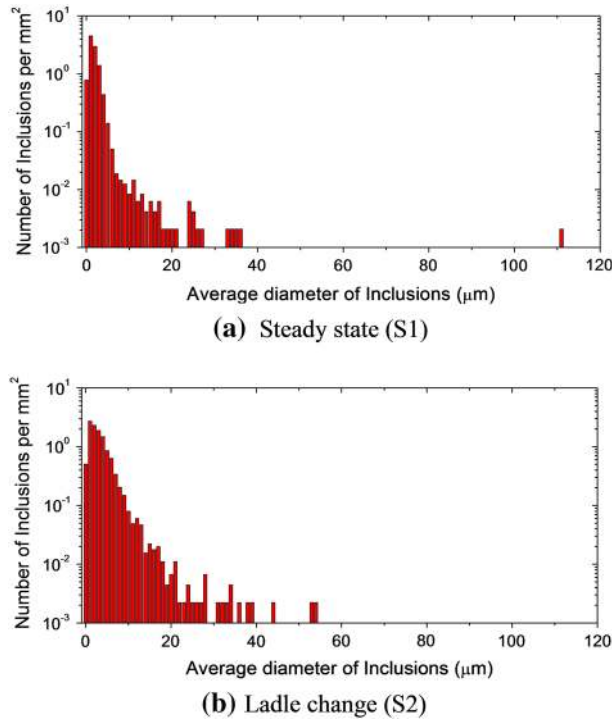


Fig. 10—Two-dimensional size distribution of oxide inclusions.

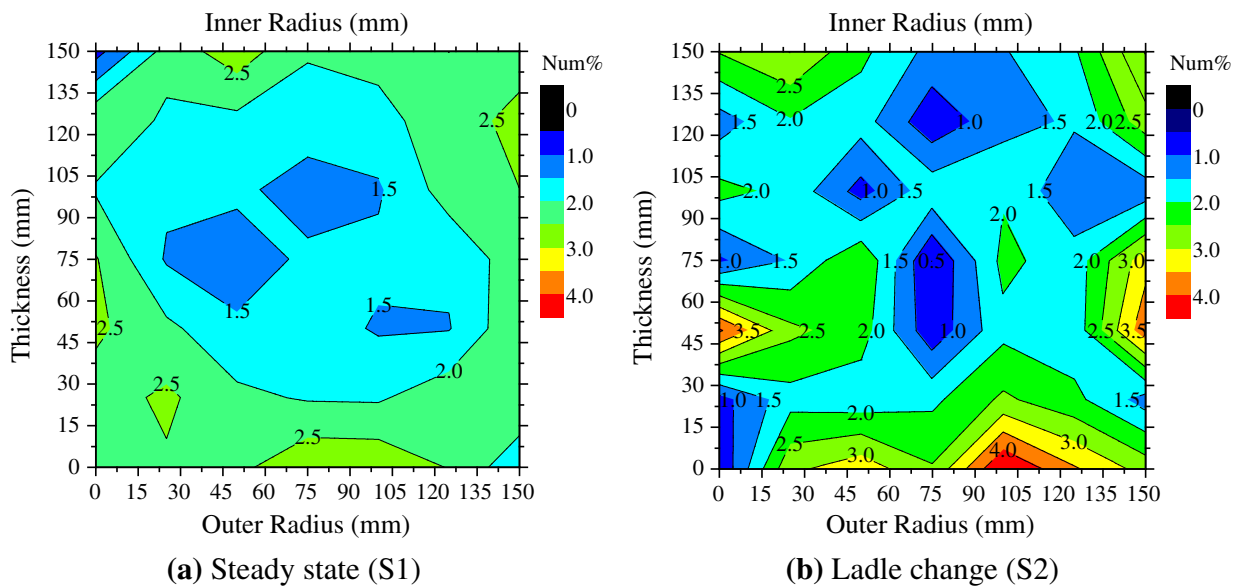


Fig. 11—Distribution of sulfide inclusions on the cross section of the billet.

(S1), there were fewer sulfide and oxide inclusions than that during the ladle change period (S2). Sulfide inclusions measured tend to accumulate at the edge of the billet (Figure 11). As shown in Figure 12, for measured oxide inclusions, there were more inclusions close to the inner radius, but there was no clear accumulation at the center of the billets; on cross section analyzed of the billet during ladle change period (S2), there were more inclusions accumulated in the center and the inner radius side of the billet. Figure 13 shows the spatial distribution of Al-Ca-Mg spinel inclusions detected on the cross section of the billets. These inclusions are scattered over the entire cross section and concentrated slightly in the center of the billet, with some deviation to the right side. The distribution of inclusions with high Na and K content is illustrated in Figure 14, no obvious distribution regularity was found in the measured cross section of the billet. Although “steady-state” case is steady casting, it has oscillatory behavior. Therefore, the distribution and the source of the inclusions can be determined more exactly by examining more different cross sections.

The number of small size inclusions was high, but small inclusions have little impact on the quality of steels. Only large size inclusions can directly lead to the failure of steel products. Therefore, the distribution of oxide inclusions measured was analyzed by different sizes. Figure 15 shows the distribution of oxide inclusions measuring 1, 5, and $>5 \mu\text{m}$ under steady casting. It indicates that $1 \mu\text{m}$ oxide particles scatter uniformly over the entire cross section, whereas 5 and $>5 \mu\text{m}$ particles tend to be concentrated at the center and on the inner radius of the billet. This pattern of entrapment of non-metallic inclusions in steel continuous casting billets was verified using mathematical simulation in our previous study.^[42] The simulation result of distribution

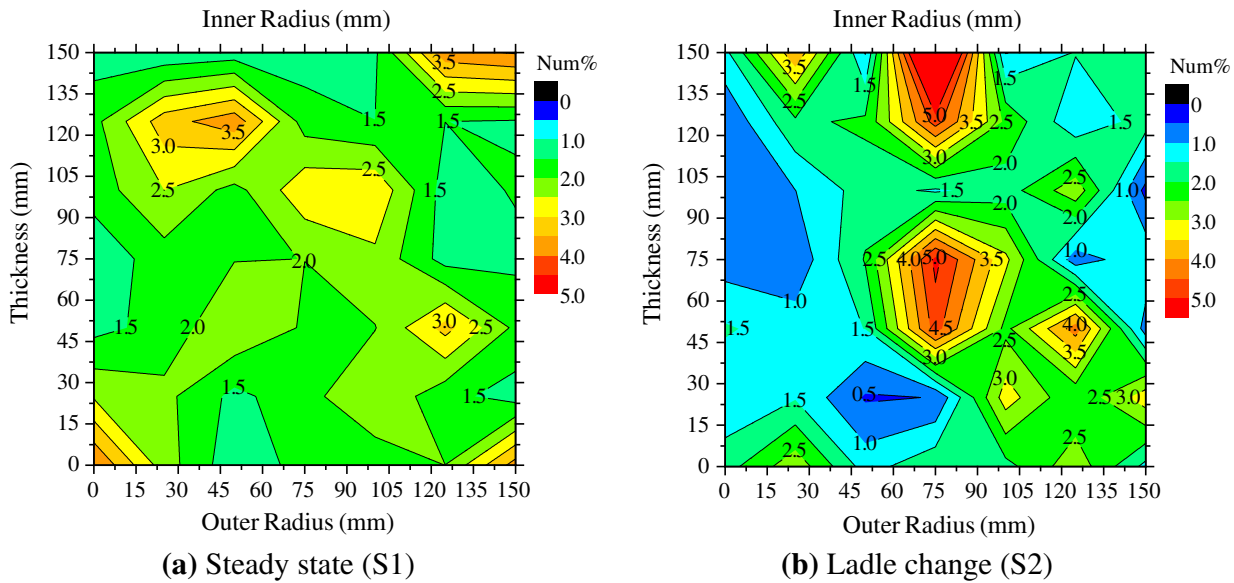


Fig. 12—Distribution of oxide inclusions on cross section of the billet.

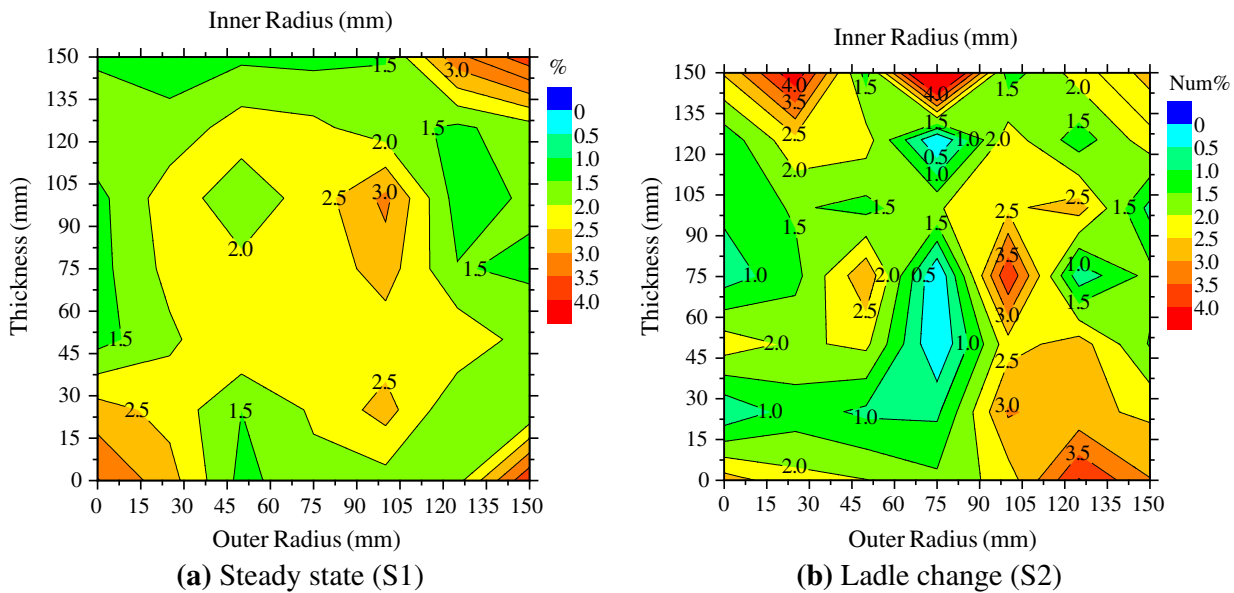


Fig. 13—Distribution of inclusion with Al, Mg, and Ca on billet cross section.

of $5 \mu\text{m}$ oxides on the cross section of the billet under steady state (S1) is shown in Figure 16. At the initial solidification, the distance between the dendrite arms can only provide space for smaller inclusions, whereas the approaching larger inclusions might be pushed away. As the dendrites grow, the dendrite spacing has the capacity to entrap much larger inclusions.

As is well known, the total oxygen can reflect the level of inclusions and cleanliness of billet. The total oxygen results directly detected by the Leco oxygen analyzer are shown in Figure 17. Under steady-state casting (S1), the total oxygen concentrated at the center of the billet and the average total oxygen was 10.3 ppm. During the ladle change period, the total

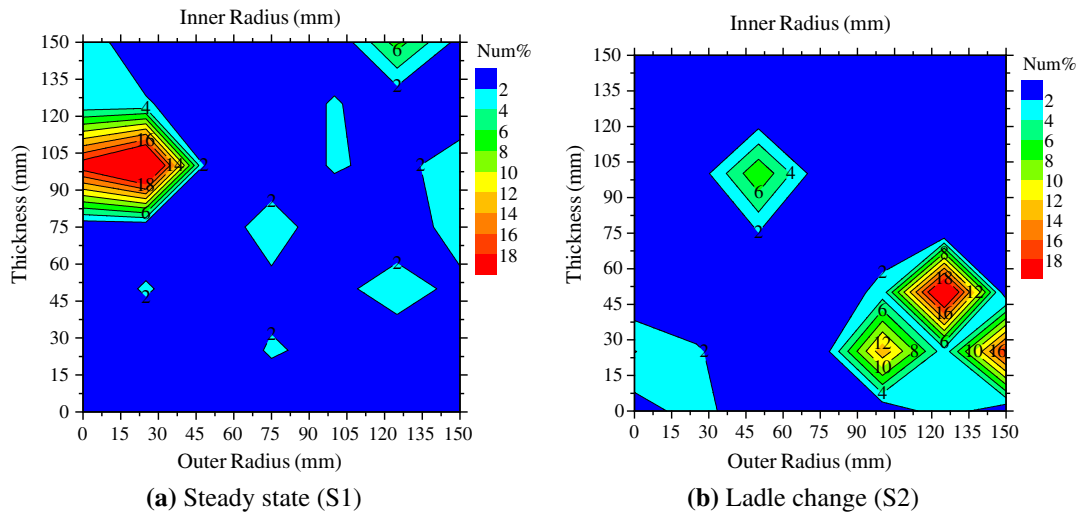


Fig. 14—Distribution of inclusion with Na and K on billet cross section.

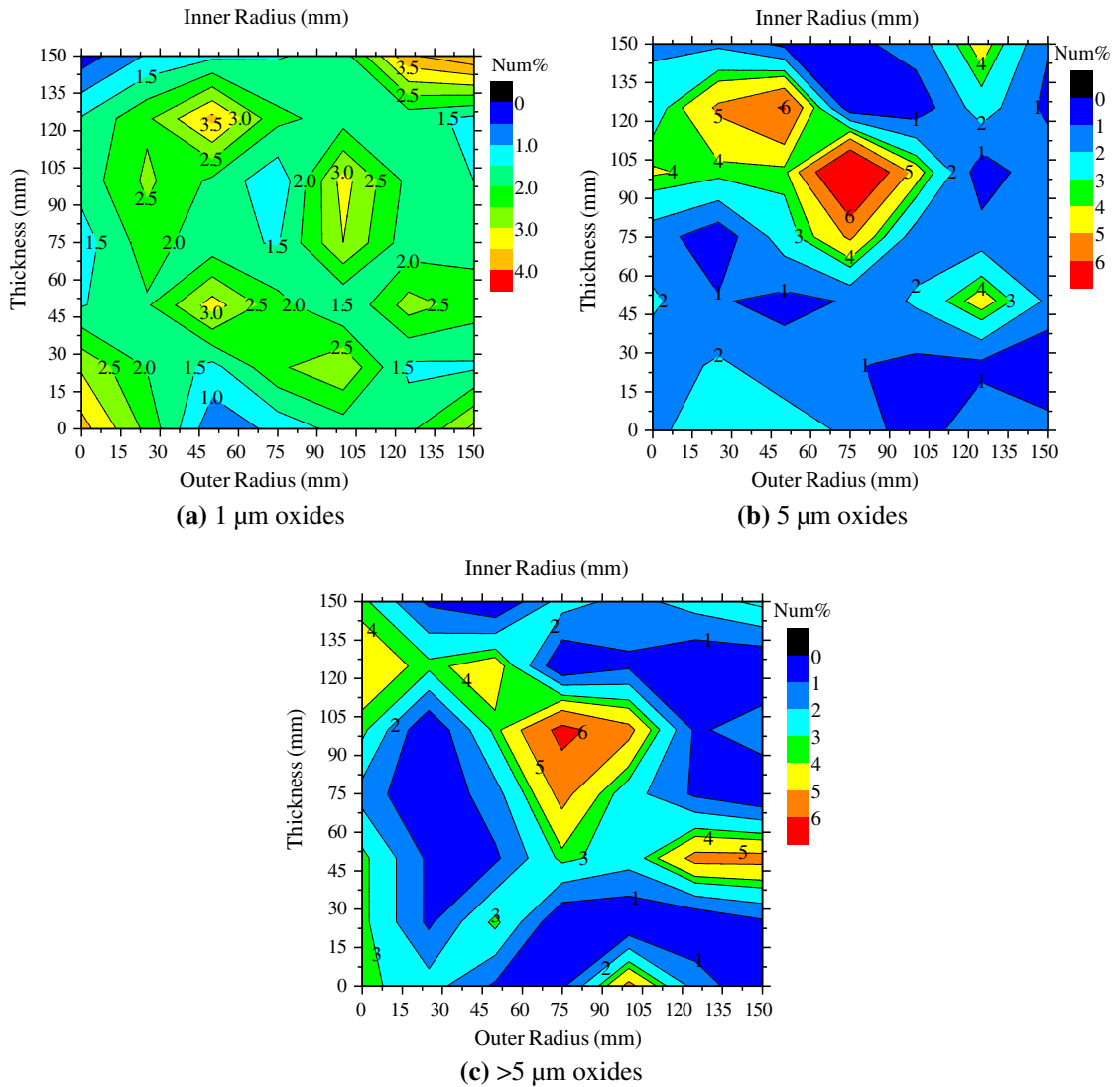


Fig. 15—Distribution of different size oxide inclusions on the measured cross section of the billet under steady state (S1).

oxygen scattered over the entire cross section and with an average value of 15.7 ppm, which was 52 pct higher than that during the steady state—an indication of increased reoxidation. Comparing the distribution inclusions by ASPEX, inclusions by calculation and the measured total oxygen, it was indicated that there was a high oxide peak close to the center of on billet cross section.

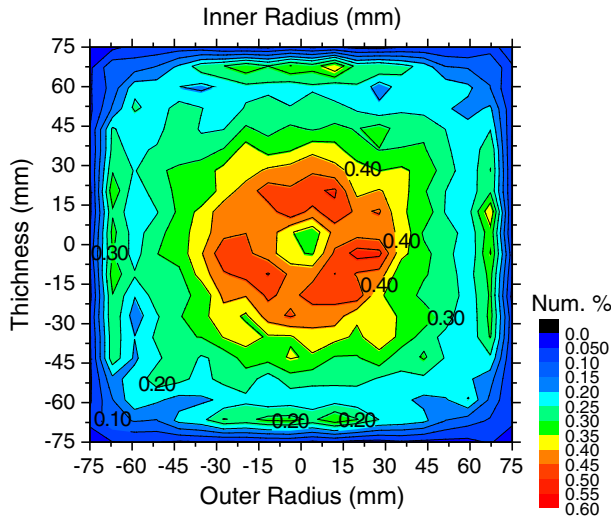


Fig. 16—Distribution of 5 μm oxides on the cross section of the billet under steady state (S1) by mathematical simulation^[42].

V. CONCLUSIONS

Automated particle analysis was applied to study the non-metallic inclusions in the entire cross section of a billet. The following was concluded:

- (1) Automated particle analysis overcomes several weaknesses of traditional measures. It provides an accurate and fast scanning in a selected area to collect information on particles, including morphology, size, spatial distribution, and composition.
- (2) Three-dimensional morphologies of typical inclusions were revealed by acid extraction. The morphology of inclusions after different time acid extractions was obtained.
- (3) The experimental results and thermodynamic calculation indicated that most oxide inclusions were solid under casting temperature with only a few in the liquid state since the refining process did not properly modify inclusions. Inclusions with high melting point can block the nozzle and have a detrimental effect on the continuous casting operation.
- (4) On the cross section of the billet under steady casting state, there were fewer sulfide and oxide inclusions than that during the ladle change period. The distributions of inclusions on the entire cross section of the billet were plotted according to inclusions type and their diameter.
- (5) On the measured cross section, total oxygen value of the ladle change period is higher than that of steady during ladle change period.

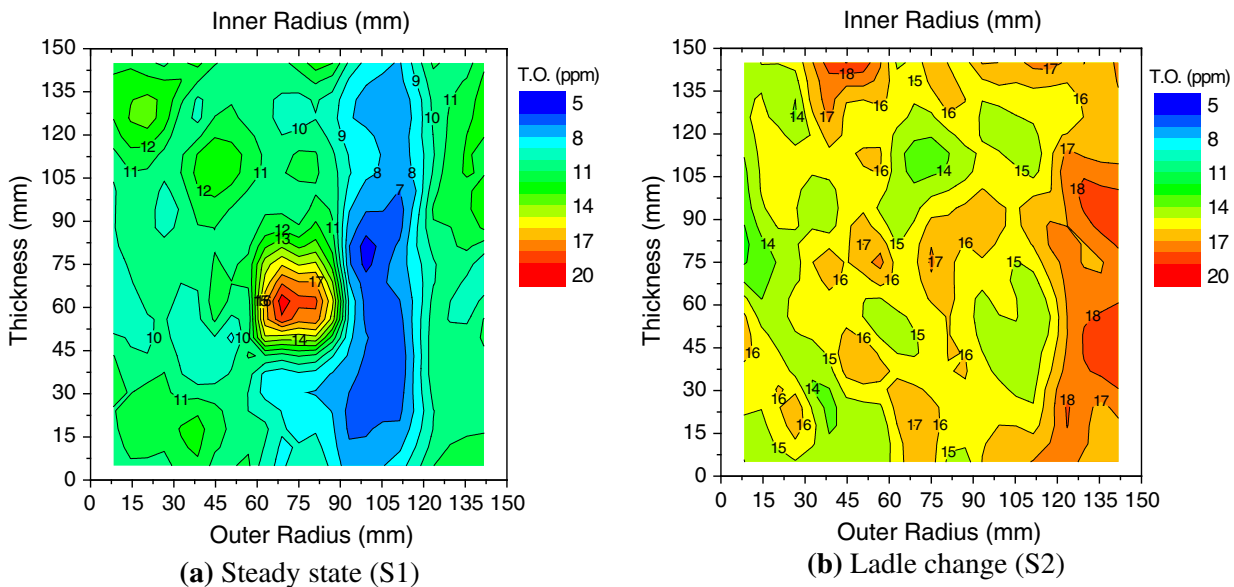


Fig. 17—Distribution of the T.O. in the billet by oxygen analyzer.

ACKNOWLEDGMENTS

The authors are grateful for support from the National Science Foundation China (Grant Nos. 51274034 and 51334002), Beijing Key Laboratory of Green Recycling and Extraction of Metals (GREM), the Laboratory of Green Process Metallurgy and Modeling (GPM²), and the High Quality steel Consortium (HQSC) at the School of Metallurgical and Ecological Engineering at University of Science and Technology Beijing (USTB), China.

REFERENCES

1. L. Zhang and B.G. Thomas: *ISIJ Int.*, 2003, vol. 43 (3), pp. 271–91.
2. T. Ehara, Y. Kurose, and T. Fujimura: *79th Steelmaking Conference Proceedings*, ISS, Warrendale, PA, 1996, vol. 79, pp. 485–86.
3. L. Zhang and B.G. Thomas: *7th European Electric Steelmaking Conference*, Venice, Italy, Associazione Italiana di Metallurgia, Milano, 2002, vol. II, pp. 277–86.
4. L. Zhang, B.G. Thomas, K. Cai, L. Zhu, and J. Cui: *ISSTech2003*, ISS, Warrendale, PA, 2003, pp. 141–56.
5. L. Zhang: *Steel Res. Int.*, 2006, vol. 77 (3), pp. 258–69.
6. L. Zhang: *J. Iron. Steel Res. Int.*, 2006, vol. 13 (4), pp. 1–8.
7. L. Zhang and B.G. Thomas: *Metall. Mater. Trans. B*, 2006, vol. 37B, pp. 733–61.
8. S. Liu, S. Niu, M. Liang, C. Li, X. Zuo, L. Zhang, and X. Wang: *Proceedings of AISTech 2007 Iron & Steel Technology Conference and Exposition*, AIST, Warrendale, PA, 2007, vol. II, pp. 771–80.
9. S. Liu, X. Zuo, L. Zhang, S. Niu, M. Liang, C. Li, and X. Wang: *Clean Steel 2007*, 2007, pp. 272–82.
10. X. Zuo, M. Long, J. Gao, Y. Wang, and L. Zhang: *Iron Steel Technol.*, 2010, vol. 7 (10), pp. 65–76.
11. Y. Ren, Y. Chen, X. Yang, S. Yang, L. Zhang, X. Ding, J. Li, S. Li, and F. Liu: *AISTech 2012 Proceedings*, 2012, pp. 1171–77.
12. Y. Ren, L. Zhang, S. Yang, and W. Yang: *AISTech 2013 Proceedings*, 2013, pp. 1159–66.
13. R. Kiessling: *Met. Sci.*, 1980, vol. 15 (5), pp. 161–72.
14. R. Rastogi and A.W. Cramb: *2001 Steelmaking Conference Proceedings*, ISS, Warrendale, 2001, vol. 84, pp. 789–829.
15. S. Li, L. Zhang, and X. Zuo: *Proceedings of Materials Science and Technology (MS&T) 2008*, AIST, Warrendale, PA, 2008, pp. 1259–69.
16. K. Kawamura, S. Watanabe, and M. Yamada: *Tetsu-to-Hagane*, 1972, vol. 58 (14), pp. 2060–66.
17. L. Zhang, S. Li, J. Wang, and X. Zuo: *Iron Steel (Chin.)*, 2009, vol. 44 (3), pp. 75–80.
18. W. Yang, X. Wang, L. Zhang, and W. Wang: *Steel Res. Int.*, 2013, vol. 84 (9), pp. 878–91.
19. J. Tan and P.C. Pistorius: *AISTech 2013 Iron and Steel Technology Conference*, May 6, 2013–May 9, 2013, Pittsburgh, PA, U.S.A., Association for Iron and Steel Technology, AISTECH, 2013, vol. 1, pp. 1301–11.
20. P.C. Glaws, R.V. Fryan, and D.M. Keener: *74th Steelmaking Conference Proceedings*, ISS, Warrendale, PA, 1991, vol. 74, pp. 247–64.
21. M. Iwasaki, N. Suzuki, T. Ohshiro, H. Utsumi, K. Miyake, and K. Sahara: *R&D Res. Dev. Kobe Steel Eng. Rep.*, 1985, vol. 35 (3), pp. 73–76.
22. R.C. Sussman, M. Burns, X. Huang, and B.G. Thomas: *10th Process Technology Conference Proceedings*, Iron and Steel Society, Warrendale, PA, 1992, vol. 10, pp. 291–304.
23. C. Bonilla: *78th Steelmaking Conference Proceedings*, ISS, Warrendale, PA, 1995, vol. 78, pp. 743–52.
24. H. Gao: *Steelmaking (Chin.)*, 2000, vol. 16 (2), pp. 38–43.
25. M. Goransson, F. Reinholdsson, and K. Willman: *I Smaker*, 1999, vol. 26 (5), pp. 53–58.
26. Q. Zhang, L. Wang, and X. Wang: *ISIJ Int.*, 2006, vol. 46 (10), pp. 1421–26.
27. <http://www.aspexcorp.com/Solutions/Software/MQAtrade.aspx>.
28. F. Schamber: *Introduction to Automated Particle Analysis by Focused Electron Beam*, ASPEX Corporation, Report, 2009.
29. V. Singh, S. Lekakh, and K. Peaslee: *62nd SFSA Technical and Operating Conference*, 2008.
30. The Japan Society for the Promotion of Science: *Steelmaking Data Sourcebook*, Gordon and Breach Science, New York, 1988.
31. B. Hallstedl: *J. Am. Ceram. Soc.*, 1990, vol. 73 (1), pp. 15–23.
32. H. Itoh, M. Hino, and S. Ban-Ya: *Metall. Mater. Trans. B*, 1997, vol. 28B, pp. 953–56.
33. H. Ohta and H. Suito: *Metall. Mater. Trans. B*, 1997, vol. 28B, pp. 1131–39.
34. K. Taguchi, H. Ono-Nakazat, T. Usui, K. Marukawa, K. Katogi, and H. Kosaka: *ISIJ Int.*, 2005, vol. 45 (11), pp. 1572–76.
35. <http://www.factsage.com/>.
36. K. Mukai, H. Sakao, and K. Sano: *ISIJ Int.*, 1969, vol. 9, pp. 196–203.
37. C. Wang, N. Verma, Y. Kwon, W. Tiekink, N. Kikuchi, and S. Sridhar: *ISIJ Int.*, 2011, vol. 51 (3), pp. 375–81.
38. D. Bouris and G. Bergeles: *Metall. Mater. Trans. B*, 1998, vol. 29B, pp. 641–49.
39. V. Brabie: *ISIJ Int.*, 1996, vol. 36 (Supplement), pp. S109–12.
40. V. Brabie: *Steel Res. Int.*, 1997, vol. 2, pp. 54–60.
41. M. Imagumbai: *ISIJ Int.*, 1994, vol. 34 (11), pp. 896–905.
42. Y. Wang and L. Zhang: *JOM*, 2012, vol. 64 (9), pp. 1063–74.